

REFINEMENT AND PERFORMANCE BENCHMARK FOR RANGE-SEPARATED WATER FORCE FIELD

PREPRINT, COMPILED JANUARY 27, 2026

Qian Gao¹, Junmin Chen^{1*}, and Kuang Yu^{1,2†}

¹Institute of Materials Research, Tsinghua Shenzhen International Graduate School (TSIGS), Shenzhen, PR China.
²Bytedance Seed - AI for Science, Shenzhen, PR China.

ABSTRACT

In our previous work, we developed a CCSD(T)-level range-separated water force field that combines the power of physics-driven and machine learning models. However, it was found that expensive CCSD(T)/CBS calculations lead to limited number of QM data as well as the missing of force labels, both of which lead to training instability issues. Bulk properties show large variations that cannot be resolved by simply reducing the fitting error in small cluster QM dataset. Such instability in bulk phase simulation is a universal problem in the training of machine learning potentials (MLPs), and is particularly severe at CCSD(T) level of theory. In this work, using our range-separated water model as an example, we aim to overcome these limitations by developing a new training workflow. It is composed by several techniques including: 1. an active learning protocol that ensures more thorough sampling in different temperatures and densities; 2. an intermediate force label technique employing machine learning density functional; and 3. an ensemble knowledge distillation (EKD) method. These techniques significantly stabilize the resulting water model, consistently achieving sub-chemical accuracies in both cluster energies and experimental properties. Benchmarks are carried out for various properties including densities, radial distribution functions (RDFs), dielectric constants, diffusivity, and infrared spectra, all showing state-of-the-art (SOTA) performances and proving the effectiveness of the training protocol.

1 INTRODUCTION

Water is one of the most common substances in nature and, despite its seemingly simple molecular structure, it exhibits a wide range of anomalous behaviors[1] arising from its complex hydrogen-bond network[2]. Therefore, water has served both as a starting point and as a stringent benchmark for testing force field development strategies. The performance of the water force field is very sensitive to the accuracy of the underlying training data[3, 4]. Therefore, ideally, one should use the gold-standard CCSD(T)/CBS level training labels to faithfully capture the intricate many-body interactions in the water system. However, CCSD(T) labels are prohibitively expensive for large molecules and periodic systems due to the notorious $O(N^7)$ scaling of CCSD(T). This poses a great challenge, as one needs to learn from a limited dataset of small clusters in vacuum, and generalize it to bulk simulation, which is a highly nontrivial task.

Until now, many works have been done to develop CCSD(T) level water force field models. The many-body expansion (MBE) approach, such as MB-pol[5, 6] and q-AQUA-pol[7, 8, 9], achieved remarkable agreement with experimental measurements of various properties. However, the complexity of PIP functions and the number of many-body terms increase rapidly with system size and chemical complexity, limiting its application in general multicomponent molecular systems. While machine learning potential (MLP) provides a promising alternative, it usually requires large amounts of energy/force data from periodic bulk-like structures, which is only affordable at the density functional theory (DFT) level. Some attempts have been made to improve the accuracy of MLPs from DFT

to CCSD(T) level: for example, transfer learning can be performed using CCSD(T) labels of very few periodic systems of affordable size[4]. Alternatively, Δ -learning can be performed targeting the difference between CCSD(T) and DFT labels for small finite clusters[10, 11]. In typical settings, pure MLPs without explicit long-range terms are local inherently and cannot correctly describe long-range interactions beyond their cutoff radius[12], so efforts have been made to incorporate long-range interactions into the MLPs, such as DPLR[13], FFLUX[14], CACE-LR[15, 16], etc.

Along this line, in our previous work[17], we proposed a range-separated water force field that carefully partitions the intermolecular interactions based on distance. The long-range interactions are described using the physics-motivated components (i.e., electrostatic, polarization, and dispersion), parameterized by rigorous TD-DFT and SAPT calculations[18, 19]. The short-range interactions are described using conventional isotropic pairwise additive terms[20] in conjunction with an anisotropic many-body machine learning (ML) correction[21], both parameterized using CCSD(T) data. The long-range part of the model adopts asymptotic parameters determined by the linear response properties of a single molecule, which is valid across various physical environments ranging from clusters in vacuum to condensed phase. Meanwhile, the ML model accounts only for short-range physics; thus, in principle it can be trained on small clusters where CCSD(T) labels are affordable. This range-separation method, later extended to the "PhyNEO" scheme, has shown excellent performance in large molecules including polymers[22, 23] and multicomponent systems such as electrolytes[24], demonstrating its great capability.

*correspondence: jmchen32@gmail.com,

kuangyu.2025@bytedance.com

However, our PhyNEO water force field was limited by poor training stability, which can be observed in more extensive bulk phase benchmarks. For sensitive bulk properties (e.g., densities, diffusivity, IR spectra), it was found that smaller errors in the QM training or validation data set do not always guarantee improvements in bulk property predictions[25]. Consequently, performing comprehensive MD benchmarks for various properties of condensed phase is essential to validate the physical fidelity of the developed potential[26]. This is especially an important issue for training at the CCSD(T)/CBS[27] level, due to the small sample size and the lack of force labels. As for CCSD(T)/CBS calculations, analytical energy gradients (forces) are often prohibitively expensive or not implemented in standard quantum chemistry packages[28, 29]. Meanwhile, previous studies show that force labels are extremely helpful in reducing the error in energy fitting [30], so the absence of CCSD(T)/CBS force can be detrimental to the development of high-level MLPs. Some work combined lower-level force and higher-level energy to train MLPs with multi-fidelity learning and achieved high accuracy[31]. However, more consistent force and energy labels are always beneficial for efficient training.

Recently, ML *ab initio* methods such as DeePKS[32], provide a feasible way to generate chemical-accuracy labels at the scaling of lower level DFT methods. Using a ML density functional, ML-DFT can learn from high-level data (e.g., CCSD(T)) and augment the data set with a comparable accuracy but with a much more favorable computational cost[33]. In this work, DeePKS is used as a surrogate model for CCSD(T) to generate cheap pretrain force data, while a transfer learning (TL) approach is used to ensure the CCSD(T) accuracy of the final model.

Besides force data from ML-DFT, we also implemented two other data augmentation techniques to enhance the stability of the final model: active learning (AL)[34] and ensemble knowledge distillation (EKD)[35]. In each cycle of AL, multiple models are trained independently using the currently available data. Trajectories are generated using the trained models and the deviations between different models are used to indicate new data points to be added into the training set. More samplings are also conducted in various temperatures and densities, so the training data achieve a better coverage over different physical conditions. Moreover, averaged predictions over all models are also generated, which are then learned by new models in an EKD procedure. We show that such an EKD approach greatly enhances the model stability in bulk property predictions. Overall, combining ML-DFT force label with AL and EKD methods, we eventually reach a much more robust training strategy. The performance and stability of the resulting hybrid water force field are demonstrated using not only cluster energies, but also various bulk properties.

We emphasize here that the problems addressed in this work are of general importance for high-level MLP development. Water is chosen as a showcase, because its anomalous bulk behaviors are well-known to be sensitive to the quality of PES. This is a typical challenging example where the CCSD(T) accuracy of PES is needed for quantitative predictions. However, high-quality data are sparse and expensive to obtain at the CCSD(T) level, which constitutes the central dilemma in modern MLP

development. The techniques used in this work, including the range-separated architecture of the PhyNEO model, the intermediate force label using ML-DFT, and the AL and EKD techniques, all contribute to the solution of this central dilemma. Only facilitated by these techniques can we obtain a SOTA water model using only 3×10^4 CCSD(T) data in clusters up to only pentamers. Therefore, the training procedure developed in this work is important in all scenarios where the availability of high-level *ab initio* data is limited.

2 METHODS

2.1 Force Field Architecture

Here, we briefly encapsulate the architecture of our PhyNEO water force field detailed in the previous paper[17]. The force field is composed of a single molecule intramolecular term and intermolecular interaction terms, as given by Eqn. 1. The intramolecular term corresponds to the spectroscopically accurate potential for a single H_2O [36] molecule. While the intermolecular interaction can be decomposed into three parts, as given by Eqn. 2, the long-range (E_{lr}) and short-range isotropic pairwise ($E_{sr,iso}$) terms described by physically motivated functions, while the short-range anisotropic term ($E_{sr,aniso}$) is represented by the Embedded Atom Neural Network (EANN)[21] model.

$$E_{tot} = E_{intra} + E_{inter} \quad (1)$$

$$E_{inter} = E_{lr} + E_{sr,iso} + E_{sr,aniso} \quad (2)$$

More specifically, long-range interactions (E_{lr}) are composed of electrostatic, polarization, and dispersion. In large distances, each term is determined by the asymptotic atomic parameters: atomic charges (q_i), multipoles (M_i), polarizabilities (α_i) and dispersion coefficients($C_{n,i}$). All these parameters can be rigorously obtained using linear response calculations (i.e., TD-DFT) in conjunction with population analysis (i.e., ISA-pol[37, 38]) and multipole expansion. These long-range terms are damped in short-range, in combination with the Born-Mayer charge penetration terms with parameters (e.g., exponents B_i and prefactors A_i) fitted to CCSD(T) data[39, 20]. The function forms of all these terms are given by the following equations:

$$E_{lr} = E_{es} + E_{pol} + E_{disp} \quad (3)$$

$$E_{es} = \sum_{i < j} M_i^T T_{ij} M_j + \sum_{i < j} f_1(B_{ij}, r_{ij}) \frac{q_i q_j}{r_{ij}} \quad (4)$$

$$B_{ij} = \sqrt{B_i B_j} \quad (5)$$

$$f_n(\lambda, r) = 1 - e^{-\lambda r} \sum_{m=0}^n \frac{(\lambda r)^m}{m!} \quad (6)$$

$$E_{pol} = \sum_{i \neq j} \mu_i^{ind} T_{ij} M_j \quad (7)$$

$$\mu_i^{ind} = \alpha_i \left(\sum_j T_{ij} M_j + \sum_j T_{ij} \mu_j^{ind} \right) \quad (8)$$

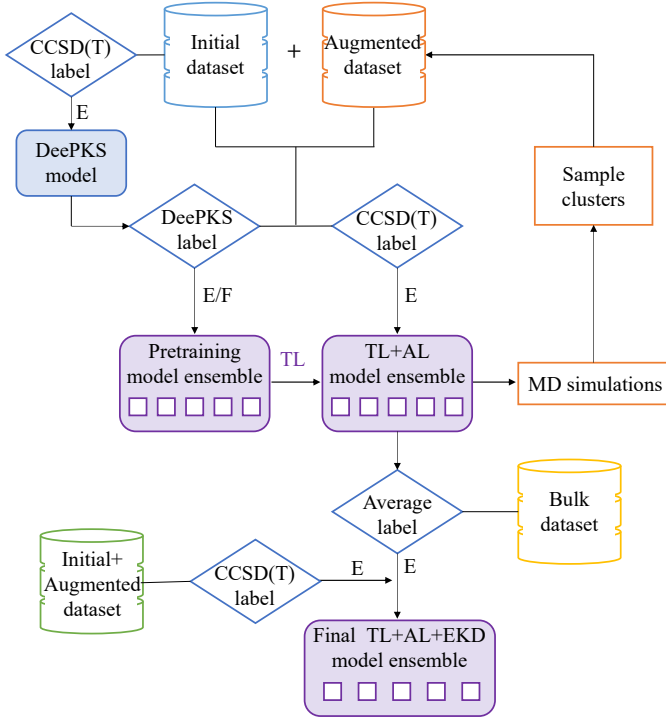


Figure 1: The workflow of the training protocol. First, a ML-DFT (DeePKS) model is trained using the initial CCSD(T) energy data and then is used to generate cheap energy/force (E/F) labels. The models are pretrained using DeePKS E/F labels and then transferred to CCSD(T) level using the original CCSD(T) E labels. Active learning using force prediction uncertainties are then conducted iteratively to generate an augmented dataset and the TL+AL model ensemble. In the final stage, the TL+AL model ensemble is distilled using bulk data to generate the final TL+AL+EKD model ensemble.

$$E_{disp} = - \sum_{i < j} \sum_{n=6,8,10} f_n(B_{ij}, r_{ij}) \frac{C_{n,ij}}{r^n} \quad (9)$$

$$C_{n,ij} = \sqrt{C_{n,i} C_{n,j}} \quad (10)$$

$$E_{sr,iso} = \sum_{i < j} A_{ij} \exp(-Br_{ij}) \quad (11)$$

The physically motivated part of the force field, including both the pairwise isotropic short-range and the long-range components, is unchanged in this work. Here, we focus on the retraining of the ML correction part ($E_{sr,iso}$) modeled by EANN. An overview of the training workflow is depicted in Fig. 1 and we will give a detailed introduction in the next section.

2.2 ML Model Training

2.2.1 DeePKS Labels

CCSD(T) force calculations are expensive, so we use DeePKS as our surrogate model for force label generation. DeePKS is a general-purpose ML Kohn-Sham functional method, that can be trained using CCSD(T) data and gives predictions at comparable accuracy but with DFT-level computational cost[32, 40]. And since DeePKS is formally a DFT calculation, it is much

more straightforward to compute force compared to naive CCSD(T). The training dataset for DeePKS model includes monomers, dimers, trimers, tetramers, and pentamers for training and validation, and hexamers, octamers, and dodecamers for testing. Training and validation configurations are randomly split with a ratio of 9:1.

In detail, the original training/validation set consists of 1421 dimers, 2214 trimers, 2090 tetramers, and 10647 pentamers, which come from our previous work[17]. Then we added 801 monomer data with geometries sampled from a 300 K PIMD simulation of a single water molecule. Furthermore, intermolecular interaction calculations often require the use of ghost atoms (i.e., off-center basis functions) to correct the basis set superposition error (BSSE)[41]. To enhance the performance of DeePKS in the calculations with counterpoise corrections, we also randomly select 10% of the data from the original training set and randomly remove some molecules to create 1639 monomers with ghost atoms.

The training of the DeePKS model was executed by iteratively calling the two procedures: solving the self-consistent field (SCF) equations and training a neural network energy functional. In the SCF calculation, we used aug-cc-pVDZ basis set. In iterative learning, the batch size was set at 16, and the total number of training epochs was set at 1500. The learning rate started at 0.0003 and decayed by a factor of 0.95 for every 300 epochs. After training for 20 iterations, we used the model in the 15th iteration as our final DeePKS model to generate training labels for the ML (EANN) part of the PhyNEO model. The choice was made to avoid overfitting since there was no significant improvement in the validation errors in subsequent iterations.

We used the final DeePKS model to calculate the total energy and force for 1408 dimers, 2193 trimers, 2072 tetramers and 9112 pentamers selected from the DeePKS training set, in total, 14785 configurations. This dataset then served as the initial pretraining dataset for PhyNEO (*vide infra*). The total energies of 500 octamers, 8 most stable hexamers and 7 most stable dodecamers were calculated to benchmark the testing performance of the DeePKS model. The performance of the final DeePKS model is shown in the Supporting Information SI.

2.2.2 Transfer Learning

After we obtained the DeePKS model at the CCSD(T) level, we pretrained the short-range anisotropic EANN term of PhyNEO, using the DeePKS energy and force data as labels. The anisotropic intermolecular interaction energy labels were obtained by subtracting the E_{lr} and $E_{sr,iso}$ terms calculated by DMFF[42] and the monomer energies calculated by MBX[43] from the total DeePKS energy, as shown in Eqn 1. Subsequently, a TL process was conducted using the original CCSD(T)-F12a/CBS intermolecular energy data. Such a TL process ensures that the final model is still at the CCSD(T) level and avoids the accumulation of errors from the DeePKS training process.

The input configurations of the training process are the DeePKS benchmark dataset mentioned above. All 14785 dimer, trimer, tetramer, and pentamer data points are used for training, while 500 octamer data points are used for validation.

During the pretraining process, we set the energy and force prefactors in the loss function to be 0.1 and 0.05, respectively, to balance the weights of energy and force. The neural network architecture contains two hidden layers with 64 neurons for each input and hidden layer. The training was carried out with a maximum training epoch of 1200. We trained 5 parallel models, forming a model ensemble. Then, with each trained model in DeePKS level as a starting point, we conducted 5 parallel TL to CCSD(T)-F12a/CBS level to obtain 5 TL models. The hyperparameters were kept the same except for the prefactor of force was set to 0 as no force labels were available at the TL stage. These training processes usually stopped within 400 epochs.

2.2.3 Active Learning

We further augmented the dataset with the AL strategy, which includes 3 iterative stages: training, exploration, and labeling.

As stated in the previous section, we first trained 5 parallel models at DeePKS level and then transferred them to the CCSD(T) level with the initial 14785 data points.

In the exploration stage, employing a randomly selected model from the 5 trained models, we conducted classical MD simulations using 512 water molecules to generate new cluster configurations. The MD simulations were conducted using the NVT ensemble, under 15 different physical conditions covering 3 temperatures, i.e., 280 K, 300 K and 320 K and 5 densities, i.e., 0.90 g/ml, 0.96 g/ml, 1.00 g/ml, 1.04 g/ml, and 1.10 g/ml. The local uncertainties of the force were then computed as shown in Eqn. 12 and 13[44] for each oxygen atom j in each selected frame i of the MD trajectories.

$$s_{ij}^{\text{local}} = \frac{1}{N_j} \sum_{n \in N(j)}^{N_j} \frac{1}{3} \sum_{k \in \{x,y,z\}} s_{in}^k \quad (12)$$

$$s_{in}^k = \sqrt{\frac{1}{N} \sum_m^N \left(F_{in}^{km} - \bar{F}_{in}^k \right)^2} \quad (13)$$

Here, the local uncertainty around the particle j (s_{ij}^{local}) is defined as the averaged atomic force uncertainties (s_{in}^k) over all its neighbors within 4 Å (denoted as $n \in N(j)$), and N_j is the number of neighbors of the particle j . The average is also conducted on all three spatial dimensions, with index k denoting the dimension (i.e., x, y, z). Meanwhile, the uncertainty of the atom force s_{in}^k is defined as the standard deviation of the force predictions among all 5 parallel models in the model ensemble. In Eqn. 13, m is the model index and $N = 5$ is the number of parallel models. F_{in}^{km} then denotes the k -component force of atom n predicted by model m in frame i , while \bar{F}_{in}^k is its average over all models.

As was previously demonstrated[44], the local uncertainty defined by the above equation is correlated with the actual local error. Therefore, we randomly selected oxygen centers with local uncertainties within the quantile range [0.950, 0.999]. Then we carved out a cluster of water around central oxygen, which includes all neighboring water molecules with an O-O distance smaller than 3.4 Å. This approximately includes the first sol-

vation shell in liquid water[2]. On the basis of these clusters, we further randomly remove redundant neighboring water molecules to obtain a balanced sampling over dimer, trimer, tetramer, and pentamer configurations.

In the labeling stage, we computed the energies and forces of the sampled water clusters using DeePKS and the energies using CCSD(T), so both the pretraining and the TL datasets are enhanced.

Finally, in the training stage, we repeated the aforementioned pretraining and TL processes at DeePKS/CCSD(T) levels to generate 5 new independent parallel models. And the exploration-labeling-training cycle was conducted for 6 iterations. Overall, 17626 new water cluster configurations were generated, including 2425 dimers, 4362 trimers, 4689 tetramers, and 6150 pentamers. Combining with the initial 14785 data points in the initial training set, it leads to a total set of 32411 data points. The analysis of the data distribution and stability tests are presented in the Supporting Information SII.

2.2.4 Ensemble Knowledge Distillation

In order to further reduce the variation of the MD simulation results given by the model ensemble, we adopted the ensemble knowledge distillation (EKD) method proposed by Gong et al.[35]. In this process, we performed 512 water simulations using 5 parallel models, in both NPT and NVT ensembles at temperatures of 277 K, 298 K, and 318 K, respectively, generating 30 simulations. For each simulation, we randomly sampled 10 frames from a 200 ps production run, generating 300 bulk frames. These 300 bulk data are then combined with the existing CCSD(T) cluster data to form the new dataset. Then all 5 parallel models are finetuned using this combined dataset so they learned the distilled information from the model ensemble.

2.3 MD Benchmarks

MD simulations for density, dielectric constant, and RDF were carried out using the PhyNEO potential implemented in the DMFF software[42] interfaced with i-PI 3.0[45]. For self-diffusion coefficients and infrared spectra, we utilized the NVT/NVE integrator from our previous work[46] instead of i-PI to propagate the dynamics. All MD simulations were performed with a time step of 0.5 fs. The MD simulations in the NPT ensemble were performed with Langevin thermostat and Bussi-Zykova-Parrinello barostat, and the MD simulations in the NVT ensemble were performed with Langevin thermostat.

To assess the MD stability of the model, we performed NPT MD simulations for all 5 parallel models in each model ensemble with 512 water molecules in a cubic box at 277 K, 298 K, and 318 K (at 1 atmosphere) and calculated the densities from the equilibrated trajectories for each model, respectively. The simulation time lengths and density values are listed in Table S5 and S6 in Supporting Information SIII. The variation of density results are then used to quantify the stability of the training process.

After verifying the stability of the training process, we chose the model with the best density performance for all following property benchmarks. The densities of liquid water were cal-

culated using 512-water MD simulations at a series of temperatures including 248 K, 268 K, 277 K, 298 K, 318 K, 338 K, and at 1 atmosphere pressure. For each temperature, the first 300 ps of the generated trajectory was considered as the equilibration process, and the rest of the trajectory was used for production analysis. Standard uncertainties were calculated using the block averaging method. Details of simulation time lengths and density values are listed in Table S7 in Supporting Information SIV.

For the calculation of RDFs, we performed MD simulation at 298 K in the NVT ensemble for 200 ps and computed the RDFs with MDAnalysis[47] from the last 100 ps trajectory after equilibration. The simulated system consists of 512 water molecules in a cubic box, with the density set to the experimental density of 0.997 g/ml.

For the calculation of the dielectric constant, MD simulations were performed in NVT at 298 K with 256 water molecules for 7.5 ns and the last 6.5 ns of the trajectory were used for the production analysis. The initial structures were extracted from the last 20 ps of a 200 ps NPT MD trajectory, for which the densities were within the standard deviation of the average density predicted by the model. Three independent simulations were performed to obtain the average value and standard deviation.

For dynamic properties, i.e., diffusion coefficients and infrared spectra, we first ran a 500 ps MD simulations with 256 molecules in the NVT ensemble at 298 K and the experimental density in 1 atm. Subsequently, we ran 30 MD NVE simulations, starting from the initial configurations uniformly drawn from the last 300 ps NVT trajectory with an interval of 10 ps. Each NVE MD simulation was performed for 20 ps and the velocities and positions were saved every 1 step. Three independent experiments were conducted to obtain the average value and standard deviation.

3 RESULTS AND DISCUSSION

3.1 Model Ensemble Performance on Water Clusters

To show the stability of the training process, we compare four model ensembles: the ones trained with the initial CCSD(T)/CBS dataset are denoted as "Initial", the ones trained with only TL and AL techniques are denoted as "TL+AL", the ones trained using the initial CCSD(T)/CBS dataset and EKD technique are labeled as "EKD", and the ones trained with both TL+AL and EKD (i.e., the full training scheme) are labeled as "TL+AL+EKD" hereafter.

We first calculated the average training and validation energy RMSE for the Initial, EKD, TL+AL, and TL+AL+EKD PhyNEO model ensembles, and list the results in Table 1. We can observe that the energy errors given by all parallel models are near sub-chemical accuracy. Comparison with DeePKS force labels is also listed in the table (further information can be found in Supporting Information Table SI). It can be seen that the force RMSEs are around $1 \text{ kcal} \cdot \text{mol}^{-1} \text{\AA}$. Compared to the Initial model ensemble, the energy and force RMSEs of the TL+AL model ensemble are slightly improved for both training and validation datasets. This can be attributed to the augmented cluster training data contributed by the TL+AL process. Oth-

erwise, it can be seen that the EKD method does not significantly improve the energy and force RMSEs of the EKD and TL+AL+EKD model ensemble, compared to their base model ensembles (Initial and TL+AL), respectively, but rather slightly worsens the results. Nevertheless, all the training and validation errors of all model ensembles are rather similar.

Table 1: The average RMSE of energy ($\text{kcal} \cdot \text{mol}^{-1} / \text{atom}$) and atomic force ($\text{kcal} \cdot \text{mol}^{-1} / \text{\AA}$) predictions of PhyNEO model ensembles for the training (denoted as *trn*) and octamer validation (denoted as *val*) set of water clusters. The RMSE^E and RMSE^F were calculated w.r.t. CCSD(T)/CBS labels and DeePKS labels, respectively.

Model Ensemble	$\text{RMSE}_{\text{trn}}^E$	$\text{RMSE}_{\text{trn}}^F$	$\text{RMSE}_{\text{val}}^E$	$\text{RMSE}_{\text{val}}^F$
Initial	0.013 ± 0.001	1.11 ± 0.01	0.019 ± 0.001	1.25 ± 0.03
EKD	0.016 ± 0.001	1.14 ± 0.04	0.021 ± 0.001	1.29 ± 0.03
TL+AL	0.011 ± 0.001	0.91 ± 0.02	0.016 ± 0.001	1.07 ± 0.02
TL+AL+EKD	0.012 ± 0.001	0.93 ± 0.04	0.017 ± 0.001	1.09 ± 0.05

In addition to the training set containing only dimers to pentamers and the validation set containing only octamers, we also examined the model performance on the most stable geometries of hexamers and dodecamers. Unlike the octamer validation set sampled from MD, this test set represents the model performance around the energy minimum. The correct prediction to the relative stabilities of these gas phase clusters also reflects the model's capability in size extrapolation.

As seen in Fig. 2, all model ensembles systematically underestimate the intermolecular interaction of hexamers and dodecamers. In comparison, the Initial model ensemble performs the best in this test set, while the TL+AL model ensemble performs slightly worse than the Initial model ensemble, and the further inclusion of EKD (i.e., TL+AL+EKD) made negligible differences. The increased error caused by TL+AL can be attributed to the increased weights of clusters extracted from bulk MD in the AL-augmented training set. A large portion of clusters in the original dataset were sampled from cluster PIMD simulations in vacuum, with structures much more similar to the low energy hexamers and dodecamers in the test set. Meanwhile, bulk MD geometries are less compact, as indicated by the larger O-O-O angle distributions [17]. Therefore, an increased portion of bulk MD geometries slightly worsens the model performance in compact water clusters in vacuum. More interestingly, directly applying EKD on the Initial model ensemble without TL+AL gives a worse performance. Nevertheless, the RMSEs of all the model ensembles are within 0.06 kcal/mol per atom, all showing sub-chemical accuracy. From the results of octamer/hexamer/dodecamer tests, it is unclear which model performs the best, but as we will show in the following sections, these model ensembles lead to significant differences in bulk simulation, thus highlighting the stability issue.

3.2 Density Variations among Model Ensemble

In Fig. 3, we compared the densities at 277 K, 298 K, and 318 K predicted by the 5 parallel models in the Initial, EKD, TL+AL and TL+AL+EKD model ensembles.

First of all, we can see that the Initial model ensemble shows up to a variation of $\pm 4\%$ in the density prediction task, which

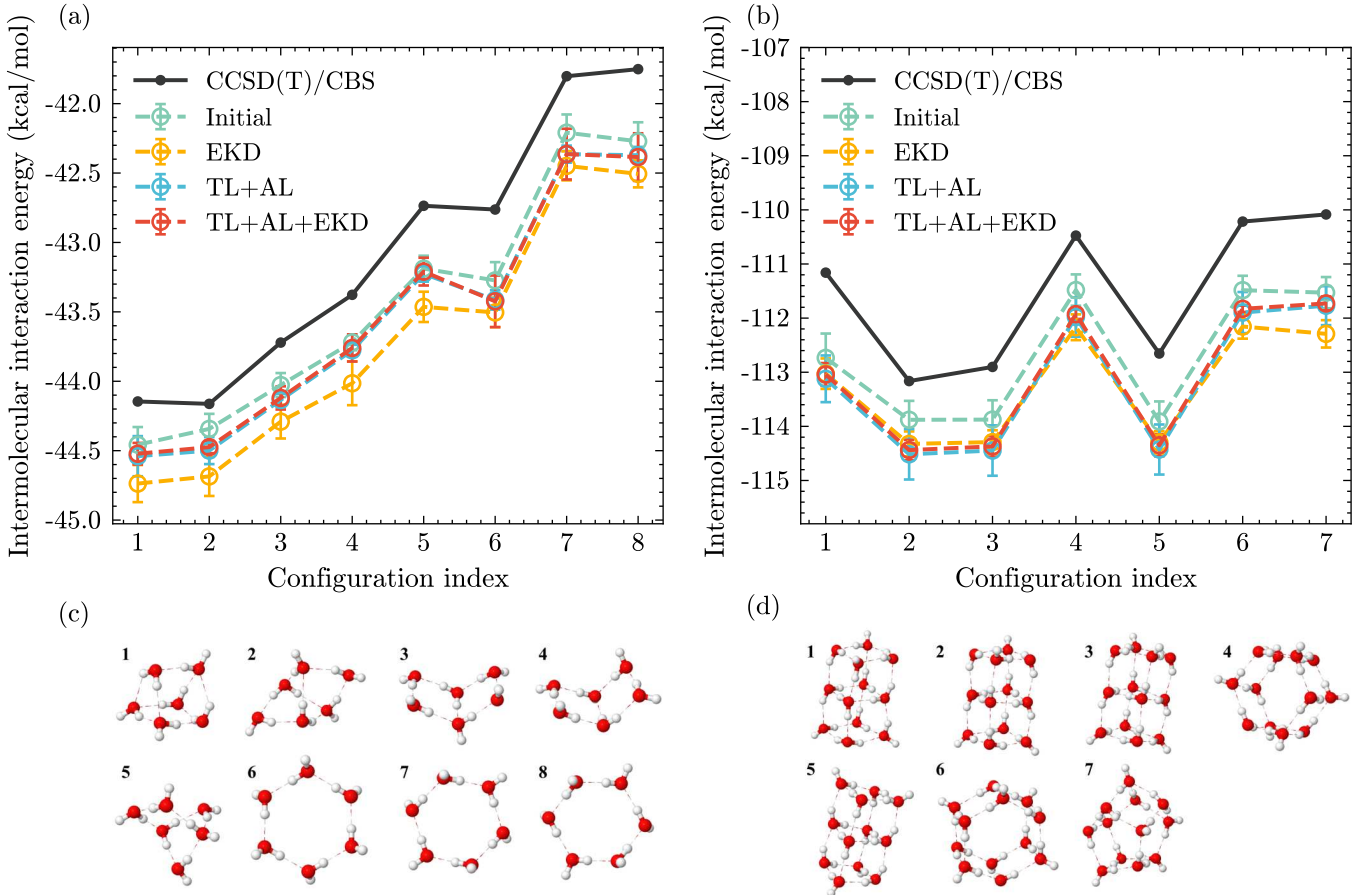


Figure 2: The intermolecular interaction energies predicted by the Initial, EKD, TL+AL, and TL+AL+EKD PhyNEO models on (a) hexamers test set and (b) dodecamers test set, compared with CCSD(T)/CBS reference. (c) The molecular structures of 8 isomers of water hexamer. (d) The molecular structures of 7 isomers of water dodecamer.

is highly unstable. The EKD ensemble features a significant reduction in model variation to approximately $\pm 1\%$, but suffers from a severe systematic underestimation of 2 – 3%. The key role of EKD can be understood as the finite QM cluster dataset does not cover all the configurations encountered in bulk MD simulation. Nontypical structures (such as structures with shortened or elongated bonds or within repulsive intermolecular regions) are hard to sample in classical MD. They may not dominate the overall distribution, but they are still thermally accessible in MD, and the large errors in these structures lead to stability issues. As shown in Fig. 3, EKD does not improve the averaged accuracy since no new physical data is introduced, but it indeed suppresses the random noises in the unsampled structures, thus improves the stability of the final model. Meanwhile, by further exploring the phase space and providing more actual E/F labels, the TL+AL model ensemble largely corrects the systematic error. However, it is still haunted by the stability issue, as indicated by the $\pm 3\%$ model variations shown in Fig. 3. In comparison, the full training scheme (i.e., TL+AL+EKD) achieves excellent performance in both accuracy and stability simultaneously. The variation of the models within the ensemble is suppressed to less than $\pm 0.5\%$, with average errors less than 1%. These results show the strong power of the combined TL+AL+EKD strategy.

Meanwhile, given the similar E/F RMSEs shown in the last section, it is clear that the fitting/validation/testing RMSEs in QM clusters are not good indicators for the quality of MLP, even though they are widely used in the current literature. Lower RMSEs in a limited QM dataset do not guarantee better performance in bulk simulations. Similar observations have been reported in a previous study[25], which investigated a number of existing MLPs and found that E/F RMSEs and bulk simulation metrics are not aligned. This inconsistency emphasizes the fact that careful benchmarks against high-quality experimental data are still indispensable.

Nevertheless, both good accuracy and stability can be achieved when TL+AL is combined with EKD, validating the training procedure proposed in this work. Considering the computational cost, hereafter, we will use the best performer in the TL+AL+EKD model ensemble for all subsequent benchmarks.

3.3 Bulk Phase Benchmarks for the Final Model

In this section, we select the best performer of the TL+AL+EKD model ensemble to carry on with our benchmarks. We calculate various thermodynamic properties (density, radial distribution function, and static dielectric constant) and dynamic properties (self-diffusion coefficient and infrared

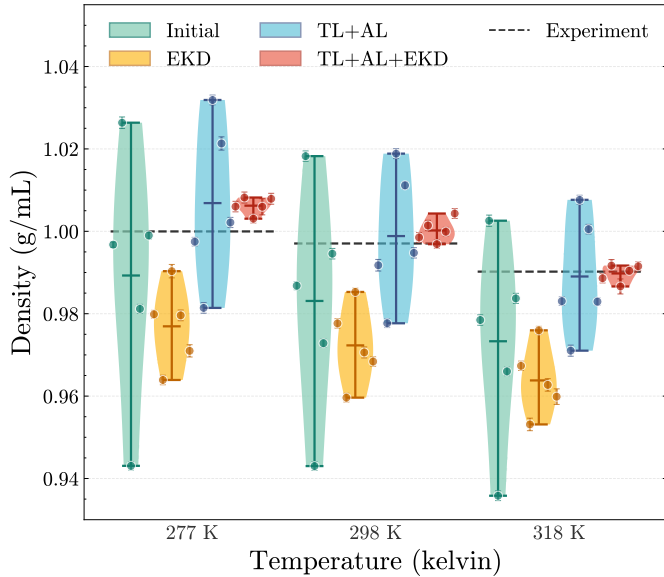


Figure 3: Comparison of the density distributions given by the Initial, EKD, TL+AL, and TL+AL+EKD model ensembles. The three groups of points and filled area from left to right correspond to simulated densities and the variations at 277 K, 298 K, and 318 K, respectively, compared with the experimental reference[48] (black dashed lines).

spectrum) of liquid water and compare them with experiments. The benchmark results are also compared with other SOTA water potentials to show the quality of the training procedure.

3.3.1 Density

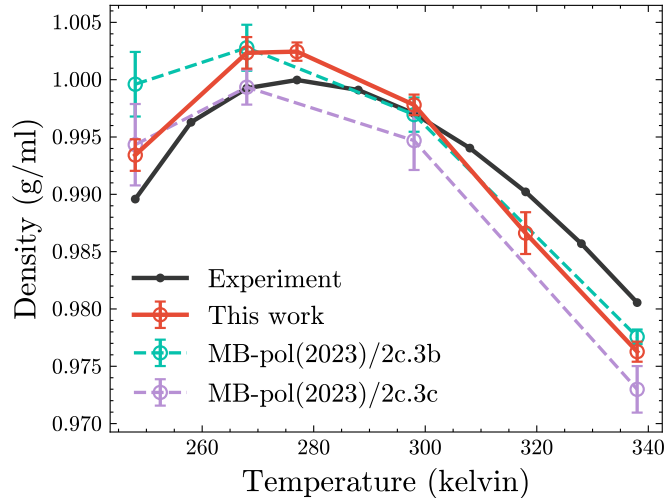


Figure 4: Densities of liquid water at 248 K, 268 K, 277 K, 298 K, 318 K, 338 K, and at 1 atmosphere predicted by the final PhyNEO model in this work, compared with experiments[48] and the reported results of MB-pol(2023)[5].

Fig. 4 shows the density as a function of temperature, in comparison to the experimental data and different versions of the MB-pol(2023) models. It can be seen that the densities agree

well with experiments within an error of 0.005 g/cm³ throughout the simulated temperature range. The densities are close to the experiment at ambient temperature (298 K), whereas slightly overestimated at lower temperatures and slightly underestimated at higher temperatures. The overall accuracy is comparable with the SOTA MB-pol models, but with much less training data (3×10^4 CCSD(T) points versus 12×10^4 CCSD(T) points). It is also encouraging to see that the density turning point at approximately 277 K is accurately captured, which is a well-known challenging task.

3.3.2 Radial Distribution Function

The OO radial distribution function (RDF) shown in Fig. 5a is generally in good agreement with the experimental measurements. Meanwhile, the OH RDF in Fig. 5b shows a more localized structure, with sharper peaks compared to the experimental measurements. This is most likely due to the negligence of nuclear quantum effects (NQE), as previous studies[50, 17, 9] indicated. Overall, the solvation structure of liquid water is well-reproduced.

3.3.3 Static Dielectric Constant

The static dielectric constant, ϵ , is calculated from the fluctuations of the total dipole moment of the system:

$$\epsilon = 1 + \frac{4\pi}{3Vk_B T} (\langle M^2 \rangle - \langle M \rangle^2) \quad (14)$$

where M is the total dipole moment of the simulation box and the angular brackets denote an ensemble average, V is the volume of the simulation box, k_B is the Boltzmann constant and T is the temperature.

The focus of this work is to develop a high-accuracy potential energy surface (PES). But to accurately calculate the dielectric properties of water, we also need a reliable dipole moment surface (DMS). It is well-known that the optimal electrostatic/polarization model for PES model cannot be used directly to predict DMS. Therefore, we employ the ML Deep Dipole model from previous work [51] to calculate the dipole moment in this work.

Table 2: Static dielectric constant of liquid water at 298 K from MD simulations with PhyNEO model in this work, compared with experiment[52] and MB-pol[53].

Potential	Classical MD	Experiment
PhyNEO model	87 ± 1	78.5
MB-pol(2016)	68.4	

The dielectric constant calculated from the MD simulations of our model (Table 2) is 11% higher than the experimental value of 78.5, while the value reported by MB-pol is 13% lower than the experimental value. Therefore, the current PhyNEO model has an accuracy comparable to that of MB-pol (with a marginal improvement). NQE may affect the simulation results, but computation of the water dielectric constants requires tens of nanoseconds of MD sampling to converge[54, 55], due to the slow dynamics of the hydrogen bond network. Such a long

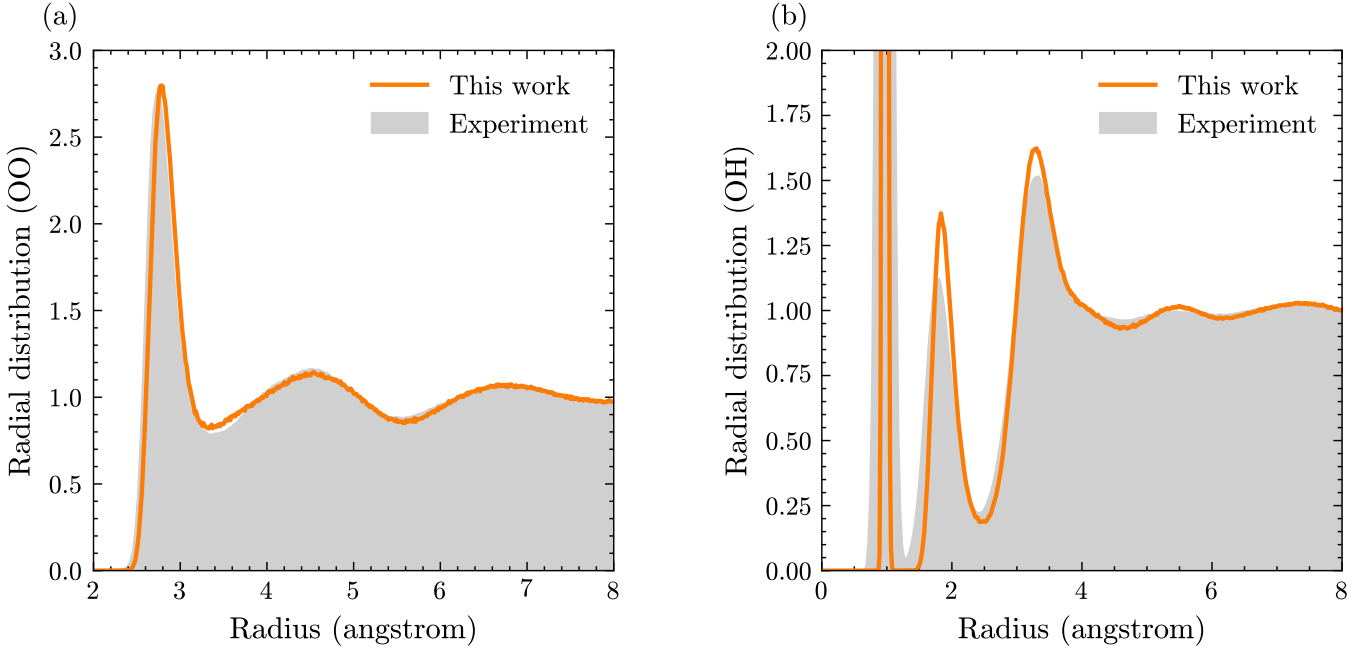


Figure 5: OO radial distribution function (panel a) and OH radial distribution function (panel b) from MD simulations at 298 K using the PhyNEO model in this work, compared with experimental data[49].

path-integral quantum MD simulation is beyond our capability. Meanwhile, experimental dielectric constants for H_2O and D_2O are numerically close[56] (78.45 versus 78.08), indicating a minor NQE on water dielectric constants.

3.3.4 Self-diffusion Coefficient

The self-diffusion coefficient of liquid water is calculated from the velocity autocorrelation function (VACF) as:

$$D = \frac{1}{3} \int_0^\infty \langle v(t)v(0) \rangle dt \quad (15)$$

where v is the velocity of the center of mass of the water molecule, and the angular bracket denotes the ensemble average.

Table 3: Self-diffusion coefficient ($\text{\AA}^2/\text{ps}$) of liquid water at 298 K from MD simulations with the PhyNEO model developed in this work, compared with experiment[57], MB-pol[53], and q-AQUA-pol[9].

Potential	Classical MD	Experiment
PhyNEO model	0.183 ± 0.003	0.230
MB-pol(2016)	0.23 ± 0.02	
q-AQUA-pol	0.185 ± 0.004	

The calculated self-diffusion coefficient (see Table 3) is underestimated compared to the corresponding experimental values. Compared to other models, PhyNEO performs worse than MB-pol, which gives an excellent description to water diffusion. Meanwhile, another SOTA CCSD(T) level water potential, q-AQUA-pol, also underestimates the self-diffusion coefficient in

classical MD. And the results between PhyNEO and q-AQUA-pol are consistent. Interestingly, a significant increase was found in the self-diffusion coefficient of water after the inclusion of NQE through the TRPMD method[8, 9], due to the competing effects of intramolecular and intermolecular NQEs[58]. Therefore, the underestimation of diffusivity is likely to be related to the negligence of NQE. Nevertheless, the accuracy of PhyNEO in water self-diffusion prediction is comparable with other SOTA water models at CCSD(T) level.

3.3.5 Infrared Spectrum

The IR spectrum is calculated from the Fourier transform of the time autocorrelation function of the system's dipole moments:

$$\alpha(\omega)n(\omega) = \frac{2\pi}{3c\kappa_BTV} \int_{-\infty}^{\infty} dt e^{-i\omega t} \langle \dot{\mathbf{M}}(0) \cdot \dot{\mathbf{M}}(t) \rangle \quad (16)$$

where $\alpha(\omega)$ is the absorption coefficient, $n(\omega)$ is the frequency-dependent refractive index, c is the speed of light in vacuum, $\dot{\mathbf{M}}(0) \cdot \dot{\mathbf{M}}(t)$ is the classical equilibrium time correlation function (TCF) of the total dipole of the system, and the angular brackets denote an ensemble average over 30 independent MD trajectories.

There are 3 major bands in the experimental infrared spectra of liquid water, including the O-H stretching absorption band at around $3000\text{-}3800 \text{ cm}^{-1}$, a peak associated with H-O-H bending vibrations at around 1650 cm^{-1} , and intermolecular librational features below 1000 cm^{-1} . Fig. 6 shows that the calculated spectrum reproduced the general features of the experimental spectrum[59]. It was demonstrated that the accuracy of both PES and DMS influences the lineshapes of the IR spectra, while PES determines the widths and positions of all spectra features, and DMS is crucial to capture the correct infrared

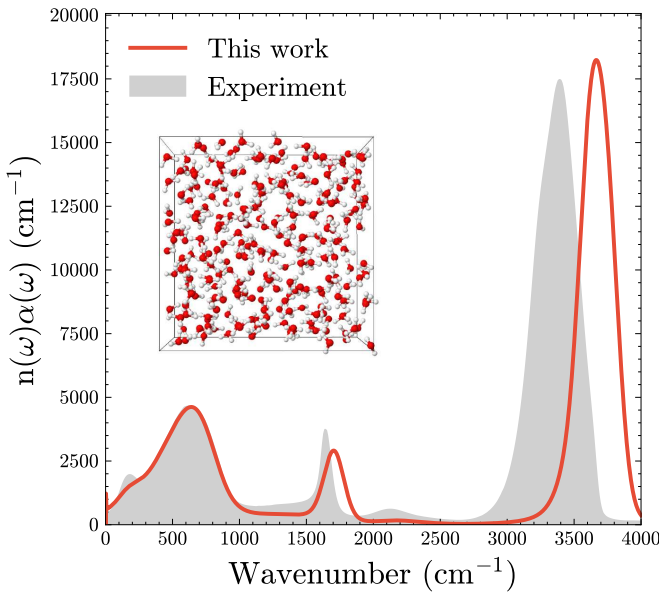


Figure 6: Infrared spectrum from MD simulations with PhyNEO model in this work, compared with experimental measurements[59].

intensity[60]. We can observe that the H-O-H bending and O-H stretching bands of the PhyNEO spectrum are blue-shifted by 50 and 250 cm^{-1} , respectively, compared to their experimental counterparts. Similar observations were reported in reference[61] by MB-pol. This is due to the neglect of NQE in classical dynamics simulations, which can be improved with quantum dynamics simulations. Meanwhile, the intermolecular librational band is in quite good agreement with the experimental measurements, showing the excellent accuracy of PhyNEO in intermolecular interactions. It is also noted that there is a small shoulder peak at around 200 cm^{-1} , which can be attributed to the charge transfer effects induced by the molecular vibration of water dimer along the OH hydrogen bond direction[62]. Although the PhyNEO model shows a small shoulder at 200 cm^{-1} , the peak intensity is largely underestimated. Given that the DMS we use in this work can reproduce this shoulder peak in other MLPs[51], we tend to attribute this problem to the reduced vibrational magnitude in the corresponding mode in PhyNEO simulation. One possible reason is the PES inaccuracies in the tightly-bounded configurations with short intermolecular distance and possibly elongated OH covalent bonds. Considering that the initial dataset was generated using the empirical q-tip4p/f potential[17], this region can be severely under-sampled. Corresponding improvement will be left to future work.

4 CONCLUSIONS

In summary, in this work we established a systematic training workflow that combines TL from intermediate ML-DFT force labels, AL, and ensemble knowledge distillation. This workflow aims to address the data deficiency and instability problem in the CCSD(T)-level MLP training. At this level, the force label is missing and the coverage of the dataset is often insuffi-

cient, making the bulk simulation results unstable even when small energy/force RMSEs in QM dataset are achieved. Using the range-separated PhyNEO water model, which is trained using limited small cluster (less than pentamer) data, we demonstrate the instability issue and justify the effectiveness of the new training protocol. The final ensemble of models reaches both good accuracy and small variation in both cluster energy and bulk density predictions. We further conducted a more comprehensive bulk benchmarks on the resulting model, showing that the final model achieves SOTA performance in various properties including density, RDF, dielectric constant, diffusivity, and IR spectrum. Meanwhile, the model is trained using much less data compared to other SOTA models, proving the efficiency of the current model and training scheme. The workflow established in this work can be beneficial to the development of more general high-level MLP models.

SUPPLEMENTARY MATERIAL

The supplementary material provides the performance benchmarks for the DeePKS model, the distribution of the AL-augmented dataset, and the numerical values of the simulated densities in the results. The CCSD(T)/CBS energy data of all dimers, trimers, tetramers, pentamers, and octamers used for the training/validation of the EANN model are available at https://github.com/plumbum082/water_force_field. Other data that were generated and used in this study are available upon request to the authors. The final PES model and the code for the training workflow and MD benchmarks are available also at https://github.com/plumbum082/water_force_field.

ACKNOWLEDGMENTS

We thank the National Natural Science Foundation of China (22473068) for the financial support of this work.

REFERENCES

- [1] Emiliano Brini, Christopher J Fennell, Marivi Fernandez-Serra, Barbara Hribar-Lee, Miha Luksic, and Ken A Dill. How water’s properties are encoded in its molecular structure and energies. *Chemical reviews*, 117(19):12385–12414, 2017.
- [2] David Eisenberg and Walter Kauzmann. *The structure and properties of water*. Oxford University Press, 2005.
- [3] Wei Tian, Chenyu Wang, and Ke Zhou. The dynamic diversity and invariance of ab initio water. *Journal of Chemical Theory and Computation*, 20(23):10667–10675, 2024.
- [4] Michael S. Chen, Joonho Lee, Hong-Zhou Ye, Timothy C. Berkelbach, David R. Reichman, and Thomas E. Markland. Data-efficient machine learning potentials from transfer learning of periodic correlated electronic structure methods: Liquid water at afqmc, ccisd, and ccisd(t) accuracy. *Journal of Chemical Theory and Computation*, 19(14):4510–4519, July 2023. ISSN 1549-9618. doi: 10.1021/acs.jctc.2c01203.

[5] Xuanyu Zhu, Marc Riera, Ethan F Bull-Vulpe, and Francesco Paesani. Mb-pol (2023): Sub-chemical accuracy for water simulations from the gas to the liquid phase. *Journal of Chemical Theory and Computation*, 19(12):3551–3566, 2023.

[6] Etienne Palos, Ethan F Bull-Vulpe, Xuanyu Zhu, Henry Agnew, Shreya Gupta, Suman Saha, and Francesco Paesani. Current status of the mb-pol data-driven many-body potential for predictive simulations of water across different phases. *Journal of Chemical Theory and Computation*, 20(21):9269–9289, 2024.

[7] Qi Yu, Chen Qu, Paul L Houston, Riccardo Conte, Apurba Nandi, and Joel M Bowman. q-aqua: A many-body ccSD (t) water potential, including four-body interactions, demonstrates the quantum nature of water from clusters to the liquid phase. *The Journal of Physical Chemistry Letters*, 13(22):5068–5074, 2022.

[8] Chen Qu, Qi Yu, Paul L Houston, Riccardo Conte, Apurba Nandi, and Joel M Bowman. Interfacing q-aqua with a polarizable force field: The best of both worlds. *Journal of Chemical Theory and Computation*, 19(12):3446–3459, 2023.

[9] Qi Yu, Chen Qu, Paul L. Houston, Apurba Nandi, Priyanka Pandey, Riccardo Conte, and Joel M. Bowman. A status report on “gold standard” machine-learned potentials for water. *The Journal of Physical Chemistry Letters*, 14(36):8077–8087, September 2023. doi: 10.1021/acs.jpclett.3c01791.

[10] Bence Balázs Mészáros, András Szabó, and János Daru. Short-range δ -machine learning: A cost-efficient strategy to transfer chemical accuracy to condensed phase systems. *Journal of Chemical Theory and Computation*, 2025.

[11] Niamh O’Neill, Benjamin X Shi, William J Baldwin, William C Witt, Gábor Csányi, Julian D Gale, Angelos Michaelides, and Christoph Schran. Towards routine condensed phase simulations with delta-learned coupled cluster accuracy: Application to liquid water. *Journal of Chemical Theory and Computation*, 2025.

[12] Oliver T Unke, Stefan Chmiela, Huziel E Sauceda, Michael Gastegger, Igor Poltavsky, Kristof T Schutt, Alexandre Tkatchenko, and Klaus-Robert Müller. Machine learning force fields. *Chemical Reviews*, 121(16): 10142–10186, 2021.

[13] Linfeng Zhang, Han Wang, Maria Carolina Muniz, Athanassios Z Panagiotopoulos, Roberto Car, et al. A deep potential model with long-range electrostatic interactions. *The Journal of Chemical Physics*, 156(12), 2022.

[14] Benjamin CB Symons and Paul LA Popelier. Application of quantum chemical topology force field fflux to condensed matter simulations: liquid water. *Journal of Chemical Theory and Computation*, 18(9):5577–5588, 2022.

[15] Bingqing Cheng. Latent ewald summation for machine learning of long-range interactions. *npj Computational Materials*, 11(1):80, 2025.

[16] Daniel S King, Dongjin Kim, Peichen Zhong, and Bingqing Cheng. Machine learning of charges and long-range interactions from energies and forces. *Nature Communications*, 16(1):8763, 2025.

[17] Lan Yang, Jichen Li, Feiyang Chen, and Kuang Yu. A transferrable range-separated force field for water: Combining the power of both physically-motivated models and machine learning techniques. *The Journal of Chemical Physics*, 157(21):214108, December 2022. ISSN 0021-9606. doi: 10.1063/5.0128780.

[18] JR Schmidt, Kuang Yu, and Jesse G McDaniel. Transferable next-generation force fields from simple liquids to complex materials. *Accounts of Chemical Research*, 48(3):548–556, 2015.

[19] Jesse G McDaniel and JR Schmidt. Next-generation force fields from symmetry-adapted perturbation theory. *Annual Review of Physical Chemistry*, 67(1):467–488, 2016.

[20] Mary J Van Vleet, Alston J Misquitta, Anthony J Stone, and Jordan R Schmidt. Beyond born–mayer: Improved models for short-range repulsion in ab initio force fields. *Journal of chemical theory and computation*, 12(8):3851–3870, 2016.

[21] Yaolong Zhang, Ce Hu, and Bin Jiang. Embedded atom neural network potentials: Efficient and accurate machine learning with a physically inspired representation. *The journal of physical chemistry letters*, 10(17):4962–4967, 2019.

[22] Junmin Chen and Kuang Yu. Phyneo: a neural-network-enhanced physics-driven force field development workflow for bulk organic molecule and polymer simulations. *Journal of Chemical Theory and Computation*, 20(1): 253–265, 2023.

[23] Chengyang Tu, Xin Li, Junmin Chen, Bo Sun, and Kuang Yu. Enhancing thermal conductivity computation of polymers via machine learning techniques. *The Journal of Physical Chemistry B*, 129(33):8593–8602, 2025.

[24] Junmin Chen, Qian Gao, Yange Lin, MiaoFei Huang, Zheng Cheng, Wei Feng, Jianxing Huang, Bo Wang, and Kuang Yu. A hybrid physics-driven neural network force field for liquid electrolytes, 2025. URL <https://arxiv.org/abs/2511.13294>.

[25] Xiang Fu, Zhenghao Wu, Wujie Wang, Tian Xie, Sinan Keten, Rafael Gomez-Bombarelli, and Tommi Jaakkola. Forces are not enough: Benchmark and critical evaluation for machine learning force fields with molecular simulations, August 2023.

[26] Junmin Chen, Qian Gao, MiaoFei Huang, and Kuang Yu. Application of modern artificial intelligence techniques in the development of organic molecular force fields. *Physical Chemistry Chemical Physics*, 2025.

[27] Asger Halkier, Wim Klopper, Trygve Helgaker, Poul Jorgensen, and Peter R Taylor. Basis set convergence of the interaction energy of hydrogen-bonded complexes. *The Journal of chemical physics*, 111(20):9157–9167, 1999.

[28] Hans-Joachim Werner, Peter J Knowles, Gerald Knizia, Frederick R Manby, and Martin Schütz. Molpro: a general-purpose quantum chemistry program package. *Wiley Interdisciplinary Reviews: Computational Molecular Science*, 2(2):242–253, 2012.

[29] Frank Neese, Frank Wennmohs, Ute Becker, and Christoph Riplinger. The orca quantum chemistry program package. *The Journal of chemical physics*, 152(22), 2020.

[30] Anders S Christensen and O Anatole Von Lilienfeld. On the role of gradients for machine learning of molecular energies and forces. *Machine Learning: Science and Technology*, 1(4):045018, 2020.

[31] Mitchell Messerly, Sakib Matin, Alice EA Allen, Benjamin Nebgen, Kipton Barros, Justin S Smith, Nicholas Lubbers, and Richard Messerly. Multi-fidelity learning for interatomic potentials: Low-level forces and high-level energies are all you need. *arXiv preprint arXiv:2505.01590*, 2025.

[32] Yixiao Chen, Linfeng Zhang, Han Wang, and Weinan E. Deepks: A comprehensive data-driven approach toward chemically accurate density functional theory. *Journal of Chemical Theory and Computation*, 17(1):170–181, 2020.

[33] Wenfei Li, Qi Ou, Yixiao Chen, Yu Cao, Renxi Liu, Chunyi Zhang, Daye Zheng, Chun Cai, Xifan Wu, Han Wang, et al. Deepks+ abacus as a bridge between expensive quantum mechanical models and machine learning potentials. *The Journal of Physical Chemistry A*, 126(49):9154–9164, 2022.

[34] Maksim Kulichenko, Benjamin Nebgen, Nicholas Lubbers, Justin S Smith, Kipton Barros, Alice EA Allen, Adela Habib, Emily Shinkle, Nikita Fedik, Ying Wai Li, et al. Data generation for machine learning interatomic potentials and beyond. *Chemical Reviews*, 124(24):13681–13714, 2024.

[35] Sheng Gong, Yumin Zhang, Zhenliang Mu, Zhichen Pu, Hongyi Wang, Xu Han, Zhaoyu Yu, Mengyi Chen, Tianze Zheng, Zhi Wang, et al. A predictive machine learning force-field framework for liquid electrolyte development. *Nature Machine Intelligence*, pages 1–10, 2025.

[36] Harry Partridge and David W Schwenke. The determination of an accurate isotope dependent potential energy surface for water from extensive ab initio calculations and experimental data. *The Journal of Chemical Physics*, 106(11):4618–4639, 1997.

[37] Alston J Misquitta and Anthony J Stone. Ab initio atom–atom potentials using camcasp: Theory and application to many-body models for the pyridine dimer. *Journal of chemical theory and computation*, 12(9):4184–4208, 2016.

[38] Alston J Misquitta and Anthony J Stone. Isa-pol: Distributed polarizabilities and dispersion models from a basis-space implementation of the iterated stockholder atoms procedure. *Theoretical Chemistry Accounts*, 137(11):153, 2018.

[39] A Hesselmann, G Jansen, and M Schütz. Density-functional theory-symmetry-adapted intermolecular perturbation theory with density fitting: A new efficient method to study intermolecular interaction energies. *The Journal of chemical physics*, 122(1):014103, 2005.

[40] Yixiao Chen, Linfeng Zhang, Han Wang, et al. Deepks-kit: A package for developing machine learning-based chemically accurate energy and density functional models. *Computer Physics Communications*, 282:108520, 2023.

[41] Neil R Kestner and Jaime E Combariza. Basis set superposition errors: Theory and practice. *ReViews in computational chemistry*, pages 99–132, 1999.

[42] Xinyan Wang, Jichen Li, Lan Yang, Feiyang Chen, Yingze Wang, Junhan Chang, Junmin Chen, Wei Feng, Linfeng Zhang, and Kuang Yu. Dmff: an open-source automatic differentiable platform for molecular force field development and molecular dynamics simulation. *Journal of Chemical Theory and Computation*, 19(17):5897–5909, 2023.

[43] Marc Riera, Christopher Knight, Ethan F Bull-Vulpe, Xanyu Zhu, Henry Agnew, Daniel GA Smith, Andrew C Simmonett, and Francesco Paesani. Mbx: A many-body energy and force calculator for data-driven many-body simulations. *The Journal of Chemical Physics*, 159(5), 2023.

[44] Esther Heid, Johannes Schörghuber, Ralf Wanzenböck, and Georg KH Madsen. Spatially resolved uncertainties for machine learning potentials. *Journal of Chemical Information and Modeling*, 64(16):6377–6387, 2024.

[45] Yair Litman, Venkat Kapil, Yotam M. Y. Feldman, Davide Tisi, Tomislav Begušić, Karen Fidanyan, Guillaume Fraux, Jacob Higer, Matthias Kellner, Tao E. Li, Eszter S. Pós, Elia Stocco, George Trenins, Barak Hirshberg, Mariana Rossi, and Michele Ceriotti. I-pi 3.0: A flexible and efficient framework for advanced atomistic simulations. *The Journal of Chemical Physics*, 161(6):062504, August 2024. ISSN 0021-9606. doi: 10.1063/5.0215869.

[46] Bin Han and Kuang Yu. Refining potential energy surface through dynamical properties via differentiable molecular simulation. *Nature Communications*, 16(1):816, 2025.

[47] Richard J Gowers, Max Linke, Jonathan Barnoud, Tyler John Edward Reddy, Manuel N Melo, Sean L Seyler, Jan Domanski, David L Dotson, Sébastien Buchoux, Ian M Kenney, et al. Mdanalysis: a python package for the rapid analysis of molecular dynamics simulations. Technical report, Los Alamos National Laboratory (LANL), Los Alamos, NM (United States), 2019.

[48] KELL GS. Density, thermal expansivity, and compressibility of liquid water from 0°C to 150°C: Correlations and tables for atmospheric pressure and saturation reviewed and expressed on 1968 temperature scale. *J Chem Eng Data*, 20(1):97–105, 1975.

[49] A. K. Soper. The radial distribution functions of water and ice from 220 to 673 k and at pressures up to 400 mpa. *Chemical Physics*, 258(2):121–137, August 2000. ISSN 0301-0104. doi: 10.1016/S0301-0104(00)00179-8.

[50] Joseph A Morrone and Roberto Car. Nuclear quantum effects in water. *Physical review letters*, 101(1):017801, 2008.

[51] Linfeng Zhang, Mohan Chen, Xifan Wu, Han Wang, Weinan E, and Roberto Car. Deep neural network for the dielectric response of insulators. *Physical Review B*, 102(4):041121, 2020.

- [52] Donald G Archer and Peiming Wang. The dielectric constant of water and debye-hückel limiting law slopes. *Journal of physical and chemical reference data*, 19(2):371–411, 1990.
- [53] Sandeep K Reddy, Shelby C Straight, Pushp Bajaj, C Huy Pham, Marc Riera, Daniel R Moberg, Miguel A Morales, Chris Knight, Andreas W Götz, and Francesco Paesani. On the accuracy of the mb-pol many-body potential for water: Interaction energies, vibrational frequencies, and classical thermodynamic and dynamical properties from clusters to liquid water and ice. *The Journal of chemical physics*, 145(19), 2016.
- [54] Gabriele Raabe and Richard J Sadus. Molecular dynamics simulation of the dielectric constant of water: The effect of bond flexibility. *The Journal of chemical physics*, 134(23), 2011.
- [55] Kehan Cai, Chunyi Zhang, and Xifan Wu. Simulations of dielectric permittivity of water by machine learned potentials with long-range coulombic interactions. *The Journal of Chemical Physics*, 163(18), 2025.
- [56] KR Srinivasan and Robert L Kay. Pressure dependence of the dielectric constant of h₂o and d₂o. *The Journal of Chemical Physics*, 60(9):3645–3648, 1974.
- [57] Manfred Holz, Stefan R Heil, and Antonio Sacco. Temperature-dependent self-diffusion coefficients of water and six selected molecular liquids for calibration in accurate 1h nmr pfg measurements. *Physical Chemistry Chemical Physics*, 2(20):4740–4742, 2000.
- [58] Scott Habershon, Thomas E Markland, and David E Manolopoulos. Competing quantum effects in the dynamics of a flexible water model. *The journal of chemical physics*, 131(2), 2009.
- [59] John E Bertie and Zhida Lan. Infrared intensities of liquids xx: The intensity of the oh stretching band of liquid water revisited, and the best current values of the optical constants of h₂o (l) at 25° c between 15,000 and 1 cm⁻¹. *Applied Spectroscopy*, 50(8):1047–1057, 1996.
- [60] Gregory R Medders and Francesco Paesani. On the interplay of the potential energy and dipole moment surfaces in controlling the infrared activity of liquid water. *The Journal of Chemical Physics*, 142(21), 2015.
- [61] Sandeep K. Reddy, Daniel R. Moberg, Shelby C. Straight, and Francesco Paesani. Temperature-dependent vibrational spectra and structure of liquid water from classical and quantum simulations with the mb-pol potential energy function. *The Journal of Chemical Physics*, 147(24):244504, December 2017. ISSN 0021-9606. doi: 10.1063/1.5006480.
- [62] Bowen Han, Christine M Isborn, and Liang Shi. Incorporating polarization and charge transfer into a point-charge model for water using machine learning. *The Journal of Physical Chemistry Letters*, 14(16):3869–3877, 2023.

Supplementary Information

Refinement and Performance Benchmark for Range-Separated Water Force Field

Qian Gao¹, Junmin Chen^{1,*}, Kuang Yu^{2,*}

¹Institute of Materials Research, Tsinghua Shenzhen International Graduate School
(TSIGS), Shenzhen, PR China.

²Bytedance Seed - AI for Science, Shenzhen, PR China.

E-mail: jmchen32@gmail.com, kuangyu.2025@bytedance.com

SI. DEEPKS MODEL PERFORMANCE

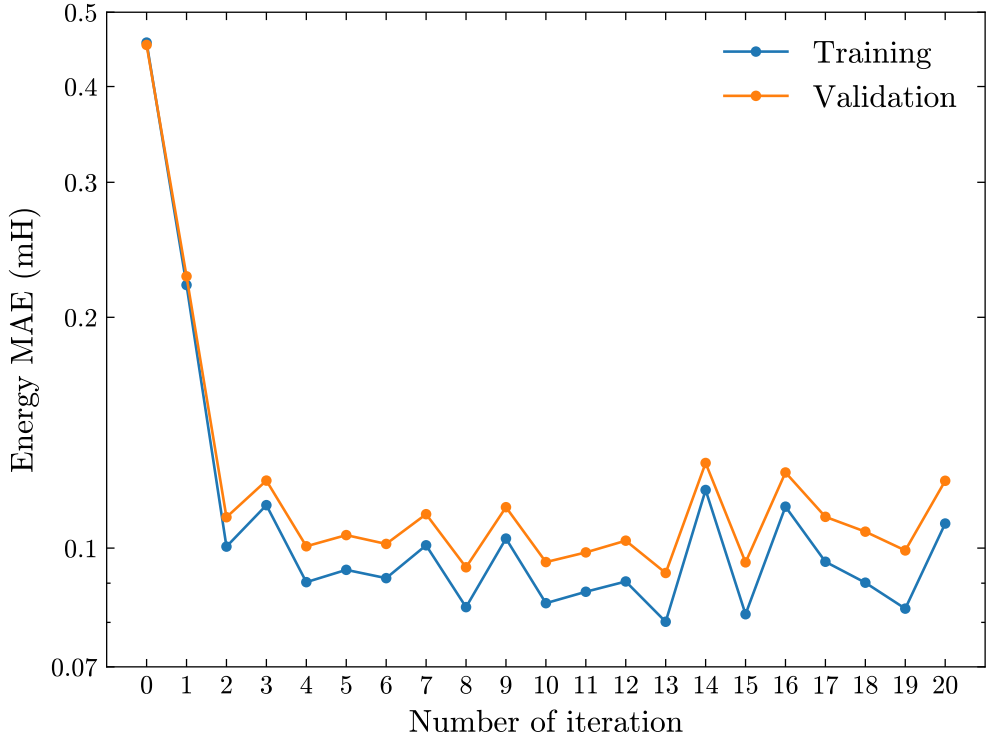


FIG. S1: Energy MAE of DeePKS model during iterative learning.

The mean absolute error (MAE) of the DeePKS model during iterative learning is shown in Fig. S1. We used the model in the 15th iteration as our final DeePKS model and benchmarked the prediction performance of total energy and force.

For energy predictions, the root mean squared error (RMSE) per atom for the selected 14785 training configurations is 0.006 kcal/mol, and that for the octamer test set is 0.013 kcal/mol, which is approximately two orders of magnitude lower than “chemical accuracy,” namely 1 kcal/mol.

TABLE S1: The RMSE (kcal · mol⁻¹/Å) of DeePKS forces for several randomly selected water clusters, compared to numerical CCSD(T)-F12(a) forces. The subscript number for dimer, trimer, tetramer, and pentamer denotes the configuration index.

dimer ₁₁₈	trimer ₇₁₀	tetramer ₁₆₅₆	tetramer ₂₀₇₁	pentamer ₁₇₅	pentamer ₆₀₇₃
0.616	0.793	0.985	0.507	1.081	0.737

For force predictions, due to the nonavailability of analytical CCSD(T)-F12(a) force for Molpro, we compared the DeePKS atomic forces with the numerical CCSD(T)-F12(a) forces calculated by Molpro. And we only benchmarked for several cluster configurations randomly selected from the training set, considering the high expense of CCSD(T) gradient calculations. It can be seen from Table S1 that the force error is approximately around 1 $\text{kcal} \cdot \text{mol}^{-1}/\text{\AA}$.

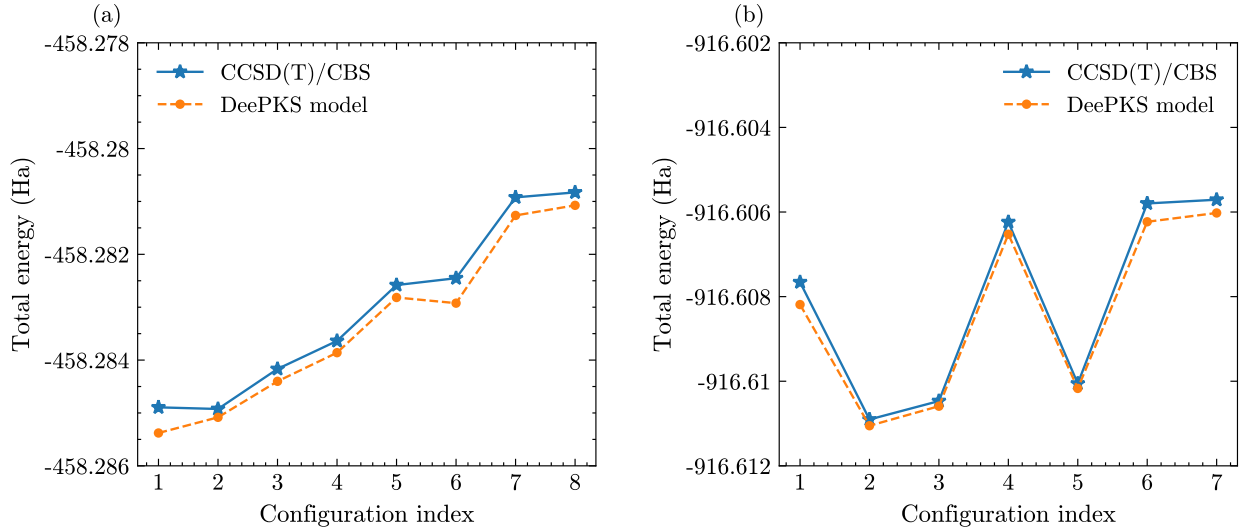


FIG. S2: Compare total energies calculated by DeePKS model and CCSD(T)/CBS method on the hexamer and dodecamer test sets.

Fig. S2 shows that the energies of the hexamer and dodecamer test sets are systematically underestimated by the DeePKS model. The RMSEs per atom for hexamers and dodecamers are 0.076 kcal/mol and 0.052 kcal/mol, respectively. The energy RMSE of the DeePKS model is at least one order of magnitude lower than chemical accuracy for stable cluster test sets and demonstrates good transferability.

SII. ACTIVE LEARNING DATA DISTRIBUTION

TABLE S2: Count of clusters with different number of monomers.

dimer	trimer	tetramer	pentamer
2425	4362	4689	6150

TABLE S3: Count of clusters sampled from MD simulation trajectories of different densities (g/ml).

0.90	0.96	1.00	1.04	1.10
2178	4382	4423	4433	2210

TABLE S4: Count of clusters sampled from MD simulation trajectories at different temperatures.

280 K	300 K	320 K
5875	5885	5866

Table S2, S3, and S4 show the constitution of sampling conditions at which water cluster candidates are sampled during active learning (AL) protocols.

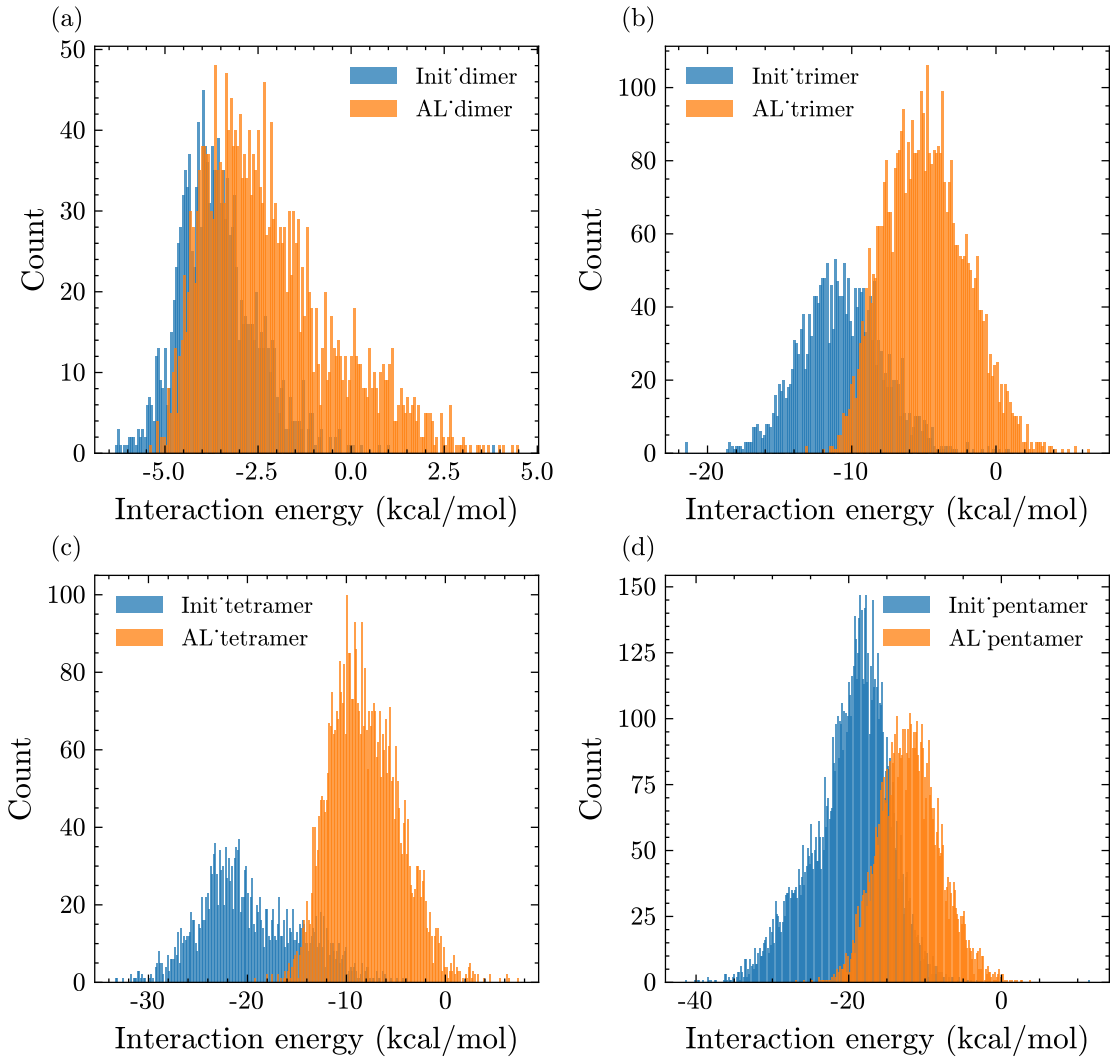


FIG. S3: The CCSD(T) intermolecular interaction energy distributions in the initial training dataset (denoted as Init) and the AL-augmented dataset (denoted as AL).

Additionally, we compared the distribution of CCSD(T) intermolecular interaction energy in the initial dataset (14785 configurations) and that in the AL dataset (17626 configurations). As seen in Fig. S3, it indicates that we have sampled more clusters with higher intermolecular energy with AL compared to the initial dataset.

SIII. SIMULATED DENSITIES BY PARALLEL MODELS

TABLE S5: The calculated densities from MD simulations with five parallel models in the Initial and the EKD model ensemble, respectively, compared with experiments[S1], and the simulation time lengths at 277 K, 298 K, and 318 K.

T (K)	Time (ns)	Initial density (g/ml)					EKD density (g/ml)					Exp. (g/ml)
		m0	m1	m2	m3	m4	m0	m1	m2	m3	m4	
277	1.5	0.997	1.026	0.943	0.981	0.999	0.980	0.964	0.990	0.980	0.971	1.000
298	1.5	0.987	1.018	0.943	0.973	0.995	0.978	0.960	0.985	0.971	0.968	0.997
318	1.0	0.978	1.003	0.936	0.966	0.984	0.967	0.953	0.976	0.963	0.960	0.990

TABLE S6: The calculated densities from MD simulations with five parallel models in the TL+AL and the TL+AL+EKD model ensemble, respectively, compared with experiments[S1], and simulation time lengths at 277 K, 298 K, and 318 K.

T (K)	Time (ns)	TL+AL density (g/ml)					TL+AL+EKD density (g/ml)					Exp. (g/ml)
		m0	m1	m2	m3	m4	m0	m1	m2	m3	m4	
277	1.5	0.997	0.981	1.032	1.021	1.002	1.006	1.008	1.003	1.006	1.008	1.000
298	1.5	0.992	0.978	1.019	1.011	0.995	0.999	1.001	0.997	1.000	1.004	0.997
318	1.0	0.983	0.971	1.008	1.001	0.983	0.989	0.992	0.987	0.990	0.992	0.990

SIV. FINAL MODEL PERFORMANCE ON DENSITY

TABLE S7: The calculated densities from MD simulations with the final model (best performer in the TL+AL+EKD model ensemble), compared with experiments[S1], and simulation time lengths at a series of temperatures.

T (K)	Time (ns)	Simulated density (g/ml)	Exp. (g/ml)
248	3.5	0.993±0.001	0.990
268	3.0	1.002±0.001	0.999
277	3.0	1.002±0.001	1.000
298	2.0	0.998±0.001	0.997
318	1.0	0.987±0.002	0.990
338	2.0	0.976±0.001	0.981

[S1] K. GS, J Chem Eng Data **20**, 97 (1975).